A buckling model for flange wrinkling in hot deep drawing aluminium alloys with macro-textured tool surfaces

Kailun Zheng, Junyi Lee, Jianguo Lin, Trevor A. Dean

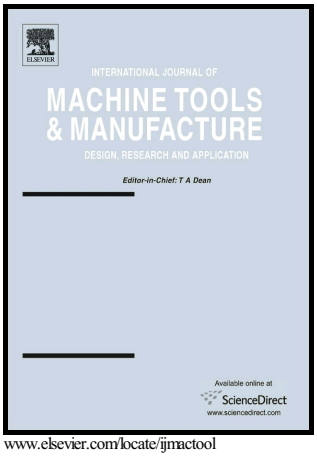

www.elsevier.com/locate/ijmactool

PII: S0890-6955(16)30172-9
DOI: http://dx.doi.org/10.1016/j.ijmachtools.2016.12.008
Reference: MTM3220

To appear in: *International Journal of Machine Tools and Manufacture*

Received date: 21 August 2016
Revised date: 10 December 2016
Accepted date: 16 December 2016

Cite this article as: Kailun Zheng, Junyi Lee, Jianguo Lin and Trevor A. Dean, A buckling model for flange wrinkling in hot deep drawing aluminium alloys wit macro-textured tool surfaces, *International Journal of Machine Tools an Manufacture,* http://dx.doi.org/10.1016/j.ijmachtools.2016.12.008

A buckling model for flange wrinkling in hot deep drawing aluminium alloys with macro-textured tool surfaces

Kailun Zheng [a], Junyi Lee [a], Jianguo Lin [a,*], Trevor A. Dean [b]

[a] Department of Mechanical Engineering, Imperial College London, Exhibition Road, London SW7 2AZ, UK

[b] School of Mechanical Engineering, University of Birmingham, Edgbaston, Birmingham B15 2TT, UK

[*]Corresponding author. Jianguo.lin@imperial.ac.uk

Abstract

The work described in this paper is the development of a buckling model based on the classical energy method of flange area material using a one-dimensional beam geometry assumption to predict flange wrinkling in hot deep drawing aluminium alloys with macro-textured blankholder surfaces. A series of deep drawing experiments utilising different macro-textured tool surfaces were performed to investigate the effects of process parameters and texture features on flange wrinkling. The results have shown that wrinkling occurs when the hollow dimension of radially grooved textures reached a certain magnitude dependent on process conditions. A dislocation-driven based damage mechanism (CDM) material model for aluminium alloys at elevated temperatures was used to model the viscoplastic behaviour during deformation. The newly developed buckling model was validated by comparison with experimental results. The predicted results showed that the resistance to wrinkling increases with increasing forming temperature and decreasing forming speed, depending on the particular viscoplastic characteristics of the work-piece. The effects of texture ratio and draw ratio on wrinkling were found to be more significant than the effects of the temperature and strain rate. The buckling model developed in this paper can be used to model the flange wrinkling phenomena, as well as the non-isothermal feature in the hot stamping condition using the macro-textured tool surfaces.

Keywords: Hot stamping, aluminium, macro-textured tool, flange wrinkling, buckling model

1. Introduction

Increasing economic and environmental concerns have driven the need for lighter but safer structures in the transportation industry, making lightweight materials, such as aluminium and magnesium alloys, popular candidates for automotive and aerospace applications [1-4]. A large proportion of body structures is made of formed sheet metal. To overcome the poor ductility of aluminium alloys at room temperature and manufacture complex-shaped components, a novel hot stamping process, named solution heat treatment, hot forming and cold die quenching (HFQ®), was proposed and patented by Lin et al. [5]. HFQ® is now a leading edge technology in this area [6, 7]. Apart from exploiting the viscoplastic behaviour of aluminium alloys at elevated temperatures, hot stamping at solution heat treatment temperatures can also increase ductility due to the dissolution of the initial coarse precipitates for heat-treatable aluminium alloys [8]. The obtained optimum microstructure can then be "frozen" using cold die quenching after hot stamping and the formed component can be artificially aged to maximum strength to meet strength requirements. The non-isothermal feature of hot stamping processes due to the heat transfer between the hot work-piece and the cold dies results in non-uniform deformations, which affect hot formability significantly. This issue can be alleviated with the use of macro-textured tool surfaces, such as the one introducted by Zheng et al. [9]. The use of textured tools significantly reduces the contact area and heat transfer compared to traditional flat tool designs. This results in a more uniform temperature distribution within the work-piece, which improves the deformation uniformity and thereby increases the drawability of hot stamping aluminium alloys.

However, tool designs with textured hollows may result in flange wrinkling for complex-shaped components that are formed under complicated stress states. The occurrence of flange wrinkling was found to be related to the dimensions of the textured hollows. To maximize the function of macro-textured tool surfaces and determine the critical texture dimensions, finite element (FE) method can be used to

model material deformation under different texture designs, which requires huge amount of simulations to obtain the critical dimension, and the accuracy also is determined by the wrinkling criterion of a particular FE software. Hence, an analytical buckling model for predicting the flange wrinkling for specific macro-textured tools would be a useful guide to facilitate wrinkling prevention by industrial tool designers efficiently and provide fundamental understanding of wrinkling occurrence.

Flange wrinkling phenomena have been investigated extensively through models by the mechanism of buckling in sheet metal forming processes. Senior [10] has established a flange wrinkling model based on the energy method for the deep drawing process without blankholder. In this model, the flange material was assumed as a one-dimensional beam and is accurate only when the flange width is small compared with work-piece radius. Yu and Johnson [11] applied the two-dimensional elastic-based rigid-plastic stability theory to analyse the flange wrinkling behaviour in the deep drawing process. The established buckling model was capable of predicting the occurrence and wave number of flange wrinkling. These buckling models applied a reduced modulus [12] to reflect the material behaviour when the stress is beyond the elastic limit, which eases the analysis at a reasonable loss of accuracy. Apart from that, Hutchinson et al. [13, 14] have also proposed a bifurcation function based on Hill's general theory of uniqueness and bifurcation of elastic-plastic solids [15] to predict the plastic wrinkling of shells. The buckling model based on the bifurcation theory can be extended further for anisotropic materials using Hill's non-quadratic yield criterion [16] and the six-component yield function of anisotropic materials [17, 18]. Besides the popular buckling models described above, a C-B wrinkling criterion based on the energy conservation principle has been proposed [19, 20]. The effects of the blankholding force were considered in the C-B criterion, and the proposed buckling models were validated by experimental results using a rectangular shaped component. The abundant buckling models in the

literature described above are focused on cold forming conditions and are inapplicable to the hot stamping processes of aluminium alloys that are gaining widespread use in recent times. The work in this paper aims to provide flange wrinkling models that are appropriate for the application of these new technologies.

The prediction of flange wrinkling for hot stamping is not trivial. Unlike materials at room temperature, viscoplastic behaviours dominate deformation at elevated temperatures, for alloys which are temperature and strain rate dependent [21]. Hence, the forming speed and thermal reaction during forming need to be considered and modelled in hot stamping processes [22]. Furthermore, the advanced macro-textured tool design used in hot stamping processes requires more factors, such as the geometry, displacement expressions, and boundary conditions, to be considered.

In this paper, a buckling model of the flange wrinkling phenomenon in hot stamping, based on the one-dimensional beam geometry assumption, using an energy method is developed the first time. This enables the occurrence of flange wrinkling to be predicted for different tool surface texture designs and the non-isothermal feature of hot stamping to be modelled. A series of corresponding deep drawing experiments have been performed to validate the developed model. In addition, the effects of forming temperature, forming speed, texture ratio, and draw ratio on the occurrence of flange wrinkling were investigated experimentally and analytically.

2. Experimental set-up

2.1 Work-piece material and experimental tool set

The selected work-piece material was commercial aluminium alloy AA6082-T6 condition provided by Smith Metal UK, which was machined to circular work-pieces with diameters: 170, 180, and 190 mm. The chemical composition of work-piece material is given in Table 1.

The components of the cylindrical hot deep drawing process using a textured tool surface are shown in Fig. 1(a). Fig. 1(b) shows the dimensions of the tools that contacted the work-piece. A flat-nosed punch, 100 mm diameter and 10 mm corner radius, was used for the deep drawing experiments, which involved different draw ratios ($DR = D_{work-piece}/D_{punch}$). The draw ratios used in the experiments were 1.7, 1.8, and 1.9. The macro-scale texture rectangular grooves were machined on only the lower blankholder. The grooves were radial so as to avoid the constraint effect of macro-textures not parallel to the material flow direction [23]. These textures can be divided into two features: the groove and the surface, as shown in Fig. 1(c), which is a plan view of a quarter of the macro-textured blankholder. The depth of each groove was 1 mm. The size of each feature is characterised by the radial angle of the groove. Surface and groove arc angles were defined as θ_S and θ_G respectively. To reflect the magnitude of texture geometry variation, a texture ratio α is defined as the ratio between the groove and surface arc angles, Eq. (1). The radial angle of the surface θ_S was 2.5 ° for all the textured tools. The ratio $\alpha = 0$ represents a non-textured flat surface, which has uninterrupted contact with the work-piece, and the ratio $\alpha = \infty$ represents a knife-edge contact with the work-piece. The blankholder was supported on a gas cushion system via a support frame, which also supplied the blank holding force. Four geometries of blankholder surface were used, a plane surface and three macro-textured surfaces. The corresponding texture ratios used in the experiments were: $\alpha = 0, 1, 3, 5$. The horizontal die surface, which was part of the blankholder, was flat. The die was attached to the ram of a 250 kN ESH hydraulic press with a maximum forming speed of 500 mm/s and a total stroke of 200 mm.

$$\alpha = \theta_G/\theta_S \quad (1)$$

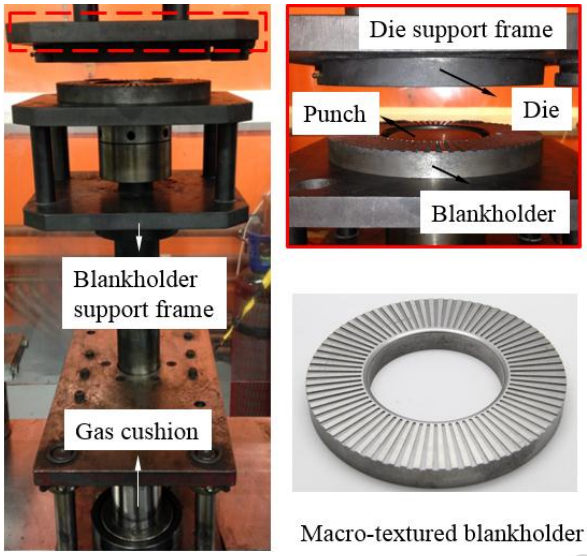

(a) Deep drawing test-rig using macro-textured blankholder

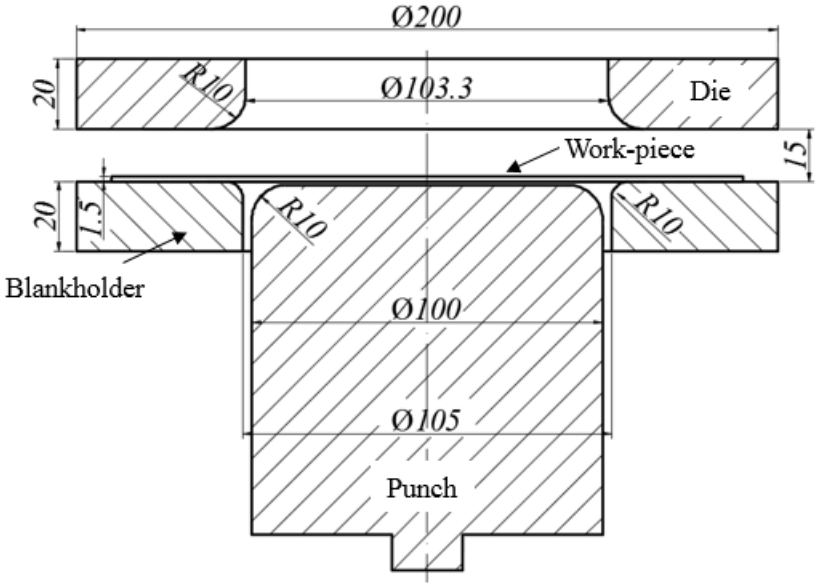

(b) Deep drawing tools and geometry

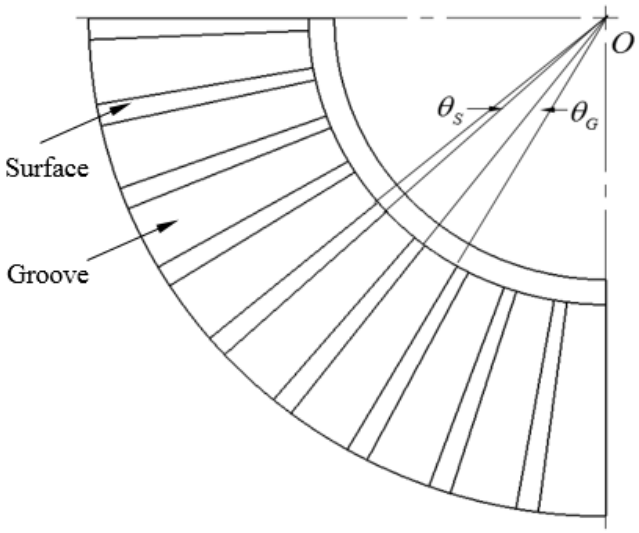

(c) Schematic diagram showing macro-textured tool surface

Fig. 1. Experimental set-up and the details of the tool

Table 1. Chemical composition of AA6082

Element	Mn	Fe	Mg	Si	Cu	Zn	Ti	Cr	Al
%	0.4-1.0	0.5	0.6-1.2	0.7-1.3	0.1	0.2	0.1	0-0.25	Balance

2.2 Experimental procedure

Fig. 2 shows the temperature profile of a work-piece during experiments. The as-received work-piece material was first solution heat treated to dissolve the initial coarse precipitates into the aluminium matrix and rapidly cooled to room temperature to obtain a super-saturated solid solution state. In order to investigate the effects of forming temperature and forming speed on flange wrinkling, the quenched work-piece was heated again to the target temperatures and deep drawn using different macro-textured blankholders at different forming speeds. Two typical forming temperatures were selected, 350 °C and 450 °C, and the forming speeds were 75 mm/s and 300 mm/s. Table 2 shows the process parameters.

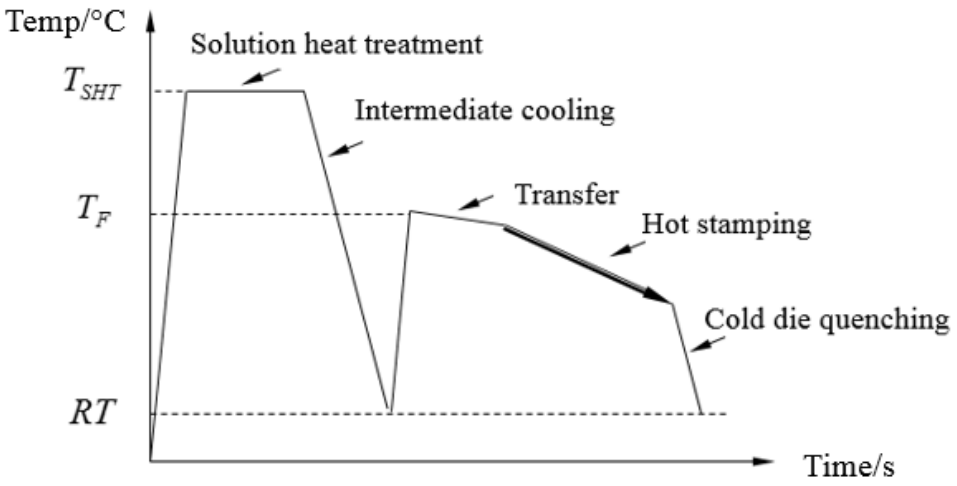

Fig. 2. The flow chart of hot stamping test procedure

Table 2. Process parameters used in this study

Process parameter	Texture ratio α	Draw ratio	Forming temperature (°C)	Forming speed (mm/s)	BHF (kN)	Tool temperature (°C)
Value	0, 1, 3, 5	1.7, 1.8, 1.9	350, 450	75, 300	10	20

2.3 Typical hot stamped parts

Fig. 3 shows typical hot stamped parts using macro-textured blankholders with different texture ratios at a forming temperature of 350 °C and a forming speed of 300 mm/s. The draw ratio was 1.8, and the blankholding force was 10 kN. As shown in the figure, the degree of flange deformation was determined by the texture ratio on the blankholder. Using flat blankholder and textured blankholder with a ratio, 1, work-piece material were successfully drawn to circular cylinders, as shown in Fig. 3(a) and (b) respectively. While severe flange wrinkling occurred for texture ratios, 3 and 5, as seen in the Fig. 3(c) and (d). The extent of wrinkling was evaluated visually.

(a)$\alpha = 0$

(b) $\alpha = 1$

(c)$\alpha = 3$

(d) $\alpha = 5$

Fig. 3. Hot stamped parts using different blankholders

Using the small texture ratio of 1, the work-piece can be successfully drawn in with a slightly wrinkled outer edge that can be ironed in, which is believed to be caused by two reasons as illustrated in Fig. 4. Fig. 4(a) shows the schematic diagram of material deformation at flange region using the textured tool design. The dash line represents the initial work-piece profile, while the red line represents the deformed work-piece profile. As the flange material experiences compressive stress in the hoop direction, thickening occurs for the flange work-piece material. When a textured tool is used, work-piece in contact with the texture surface is constrained by the blankholding force, while the work-piece located at the texture hollow has no blankholding force constraint. Therefore, the thickening is greater for the material at the texture hollow

which results in a wave profile as shown in the red line in Fig. 4(a). Furthermore, as the outside flange material undergoes the maximum compressive stress, the thickening there is greater than the inner flange material, as can be seen in Fig. 4(b). Such a wave pattern can be further ironed by the punch and die when the work-piece material is drawn fully in the die. The other possible reason is that, when the work-piece material is drawn to a large radius reduction, slight wrinkling occurs at the outside edge of the flange which can be ironed also. Compared to the severe flange wrinkling using texture ratios 3 and 5, the slight wrinkling using a texture ratio of 1 has no effect on the draw-ability of the hot stamping process. To enable tools to be designed with textures that optimally control heat transfer and do not cause unacceptable wrinkling, an accurate model of the process is necessary.

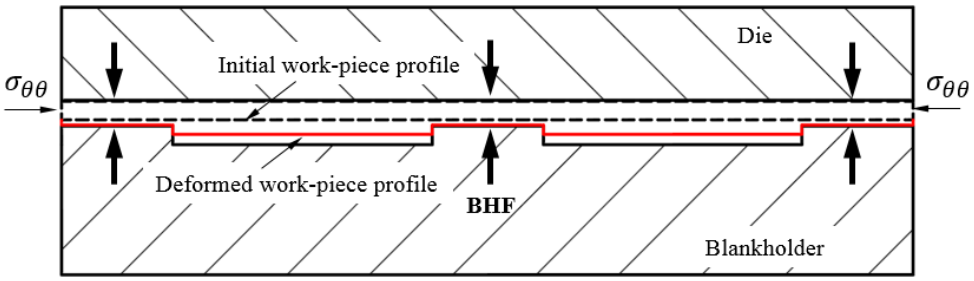

(a) Schematic diagram of work-piece deformation at flange zone

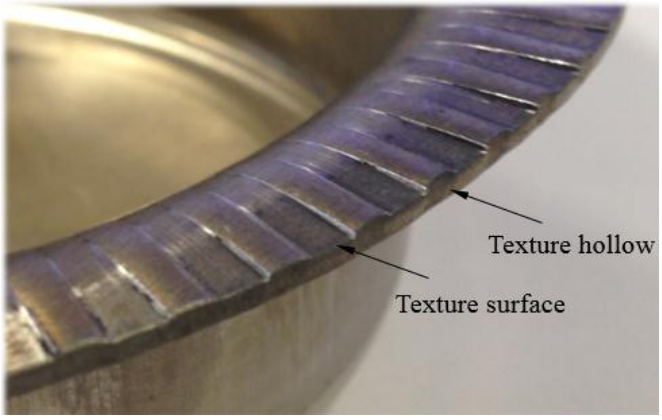

(b) Flange material deformation

Fig. 4. Flange material deformation textured blankholder with a texture ratio, $\alpha = 1$

3. Buckling model

3.1 Modelling of macro-textured tool surface design

Since the wrinkling phenomenon is affected by the texture geometry, the texture geometry and the corresponding work-piece are defined for this model. Fig. 5 shows the outer edges of part of a textured blankholder. The area of the work-piece within the blankholder has been divided into two zones: Zone G subtends a groove and Zone S contacts the blankholder surface. Thus the work-piece area within the blankholder is divided into a series of discrete sectors, the sector reprsenting Zone S has a same subtended radial angle with the surface of tool texture, θ_S, while the sector reprsenting Zone G corresponds to a radial angle θ_G. The magnitudes of θ_S and θ_G are the same as those used in the experiments.

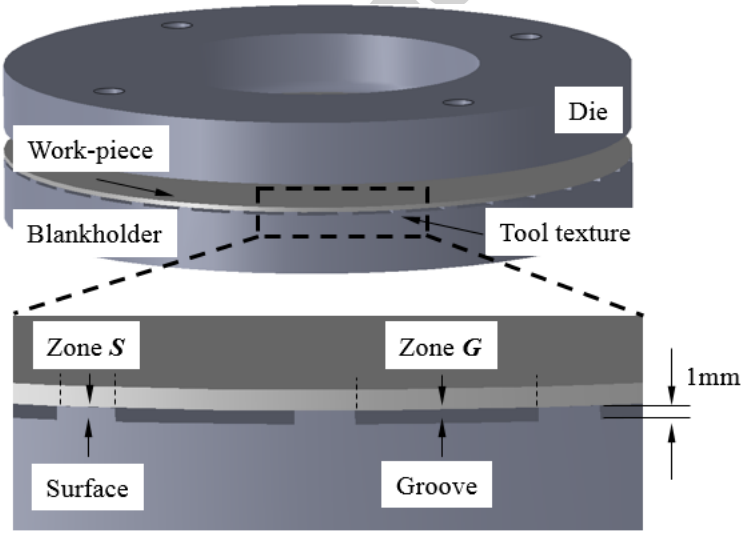

Fig. 5. Zoning of tool textures and work-piece

3.2 Modelling of work-piece material in hot stamping condition

To model the work-piece material deformation of AA6082 at elevated temperatures, a viscoplastic damage constitutive model, which accounts for the mechanisms of dislocation-driven evolution phenomena, hardening, dynamic and static recovery, and damage, has been developed. The full set of the constitutive equations are listed as follows:

$$\dot{\varepsilon}^P = \left(\frac{\sigma/(1-\omega)-R-k}{K}\right)^{n_1} \tag{2}$$

$$\dot{R} = 0.5B\bar{\rho}^{-0.5}\dot{\bar{\rho}} \tag{3}$$

$$\dot{\bar{\rho}} = A(1-\bar{\rho})|\dot{\varepsilon}^P| - C\bar{\rho}^{n_2} \tag{4}$$

$$\dot{\omega} = \eta_1 \frac{|\dot{\varepsilon}^P|^{\eta_2}}{(1-\omega)^{\eta_3}} \tag{5}$$

$$\sigma = E(1-\omega)(\varepsilon - \varepsilon^P) \tag{6}$$

Eq. (2) is the traditional power-law viscoplastic flow formulation, which considers the effects of damage ω on viscoplastic flow. Eq. (3) represents the evolution of material hardening, R, which is a function of the normalised dislocation density $\bar{\rho}$ defined by $\bar{\rho} = (\rho - \rho_i)/\rho_m$, where ρ_i is the dislocation density of the material at the initial state and ρ_m is the maximum (saturated) dislocation density of the material. Hence, the range of normalised dislocation density, $\bar{\rho}$, is from 0 to 1. Eq. (4) represents the rate of accumulation of dislocations. Eq. (5) represents damage evolution for the uniaxial formulation, which is a function of plastic strain rate $\dot{\varepsilon}^P$. Eq. (6) is Hook's law for a simple uniaxial state. In this equation set, n_2 and η_3 are temperature-independent parameters, while the material parameters K, k, n_1, B, A, C, E, η_1, and η_2 are temperature dependent. The equations of these parameters were developed based on the Arrhenius equation and other functions for modelling aluminium alloys at elevated temperatures by Mohamed et al. [7, 24] , which are defined as follows.

$$K = K_1 \exp(K_2/T) + K_3 \exp(K_4/T) \quad (7)$$

$$k = k_1 + (k_2 - k_1)/(1 + (1/(k_3 T))^{k_4}) \quad (8)$$

$$n = n_{11} + n_{12} \exp(-(n_{13}/T)) \quad (9)$$

$$B = B_1 + (B_2 - B_1)/(1 + (1/(B_3 T))^{B_4}) \quad (10)$$

$$A = A_1 \exp(A_2/T) + A_3 \exp(A_4/T) \quad (11)$$

$$C = C_1 \exp(C_2/T) \quad (12)$$

$$E = E_1 \exp(E_2/T) \quad (13)$$

$$\eta_1 = \eta_{11} + (\eta_{12} - \eta_{11})/(1 + (1/(\eta_{13} T))^{\eta_{14}}) \quad (14)$$

$$\eta_2 = \eta_{21} + (\eta_{22} - \eta_{21})/(1 + (1/(\eta_{23} T)^{\eta_{24}})^{\eta_{25}} \quad (15)$$

Table 3 lists the values of material constants for the viscoplastic damage model of AA6082 for the conditions relevant to hot stamping. In Table 3, the symbol X represents the temperature-dependent parameter in Eq. (2) to Eq. (6). X_1 to X_5 represent the corresponding components of each temperature-dependent parameter. The values of material parameters were obtained by fitting hot uniaxial tensile test results of AA6082 at different temperatures [25] via a computer-based methodology and reasonable the obtained values experientially based on the viscoplastic behaviours of aluminium alloys, as shown in Fig. 11(b). A genetic algorithm (GA)-based optimisation method [26] is used for the determination of the constant values within the material model using the objective functions given in [27].

Table 3. Material constants for viscoplastic damage model of AA6082. The variable X at the top of the table represents the property listed on the first column.

X	X_1	X_2	X_3	X_4	X_5
K	24.61	214.4	-3124	-3819	
k	99.014	7.59901	0.0017	7.4075	
n_1	-19.068	16.007	-224.69		
B	454.99	37.28519	0.0021	10.404	
A	50.71	-2300	2.903	-316.9	
C	11890	-5004			
E	10870	555.0216			
η_1	0.30515	0.09066	0.001765	10.611	
η_2	1.03	0.961	0.00153	56.2013	35
η_3			17		
n_2			1.8		

3.3 Modelling process parameters

In hot stamping processes, temperature and strain rate of the work-piece material are related to the forming speed and temperature evolution resulting from the non-isothermal feature of hot stamping, which further affect viscoplastic behaviour. Temperature and strain rate vary in different regions with time during forming, which results in a variation of material stress-strain behaviour, which can influence buckling characteristics. Hence, to model the occurrence of flange wrinkling, the strain rate and temperature evolution determined from the forming speed and initial

forming temperature needs to be found and used as the inputs to the viscoplastic material model.

3.3.1 Strain rate modelling

Strain rate evolution is dependent on forming speed. To calculate the relative strain rate, the first step is to calculate the strain of work-piece material, especially the Zone G material, which may experience buckling. In the circular deep drawing process performed in this study, the flange material normally experiences a compressive hoop stress, $\sigma_{\theta\theta}$, and a tensile radial stress, σ_{rr}, as shown in Fig. 6(a). Since only the region (Zone G) that is not in contact with the tool, denoted by the unshaded region in Fig. 6(a), is of interest for the buckling analysis, the friction between the work-piece and tool can be neglected. The mathematical expressions of the stress state, with no buckling, within Zone G using the Tresca yield criterion are as follows.

$$\begin{cases} \sigma_{rr} = \sigma_f \ln(b/r) \\ \sigma_{\theta\theta} = \sigma_f [\ln(b/r) - 1] \end{cases} \tag{16}$$

where σ_f is the material flow stress, b is the work-piece outer radius, and r is the instant radius of an infinitesimal unit.

According to Eq. (16), the magnitude of the compressive hoop stress is maximum at the outer radius of the work-piece. The hatched arc regions in Fig. 6(a) represents an infinitesimal fibre located at the outer radius of work-piece at different time moments suggesting that the wrinkling initiates here. Therefore, the strain and strain rate of this region at a given time are used as input parameters to the material model. Furthermore, the radial stress on the material at the outer radius is zero, so that only the stresses in the hoop direction need to be calculated. These features allow the analysis to be simplified by treating the region at the outer radius as a fibre being compressed uniaxially in the hoop direction as suggested by Baldwin et al. [28]. In a

uniaxial compression, as the angle θ_G is fixed. Then, the strain can be defined as $\varepsilon = dr/r$, then the strain rate is the rate of change of the radius divided by the instantaneous radius, which is a function of time, as given in Eq. (17). The total strain is then found by integrating the strain rate with respect to time in Eq. (17). This integration enables to find the true strains using the ram speed, which aims to establish a relationship between actual forming process and material stress-strain curves.

$$\begin{cases} \varepsilon = \int_0^t \dot{\varepsilon}\, dt = \int_0^t \frac{1}{r(t)} \frac{\partial r(t)}{\partial t}\, dt \\ \dot{\varepsilon} = \frac{1}{r(t)} \frac{\partial r(t)}{\partial t} \end{cases} \tag{17}$$

where t is the time.

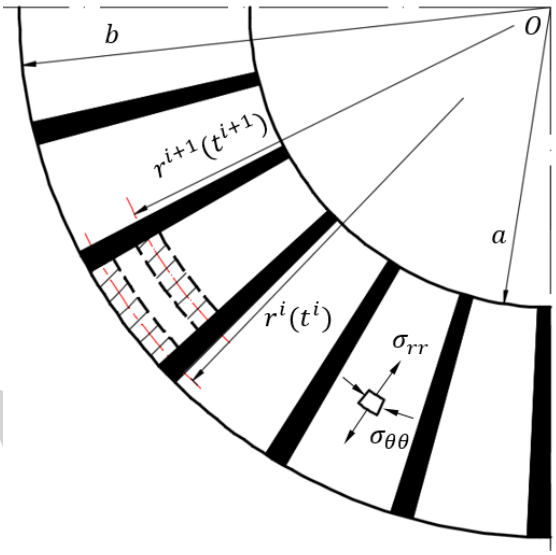

(a) Stress state of flange region

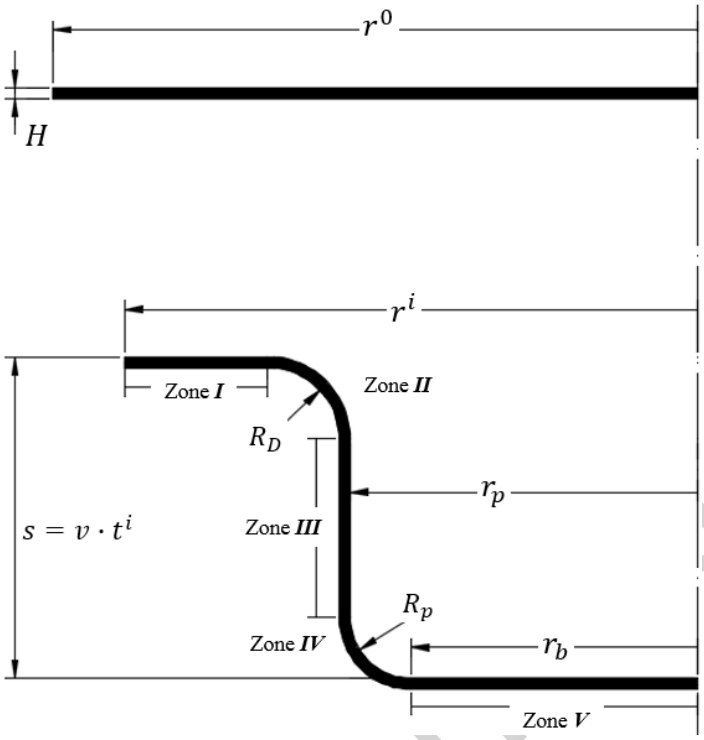

(b) An instant during forming

Fig. 6. Zoning of work-piece material during forming

The strain and strain rate in Eq. (17) can be found by considering the forming speed of the work-piece. In the experiments and model, a constant forming speed was used. The press stroke varies linearly with time and can be calculated using Eq. (18).

$$s = vt + s_0 \tag{18}$$

where s is the stroke, s_0 is the stroke at $t = 0$, and v is the forming speed of the punch, which is a constant and same with the parameters in the experiments.

The geometry of formed part at an instant moment during deformation is shown in Fig. 6(b) and the flange outer radius can be expressed in terms of the forming speed and time. Since the material undergoes plastic deformation for the majority of the deformation process, the work-piece is assumed to have a constant volume, which

enables the radius to be found from the initial volume using the following equation. Subsequently, the strain and strain rate can be calculated.

$$V_0 = H \cdot \pi \cdot (r_0^2) = V_I + V_{II} + V_{III} + V_{IV} + V_V \quad (19)$$

where V is the volume, H is the thickness, the subscript 0 denotes the initial value and the subscripts I, II, III, IV, and V denotes the zones classified in Fig. 6(b). The volumes of the individual zones in Fig. 6(b) are defined by the following equations by assuming that the thickness H of the work-piece is constant which enables to simplify the calculation significantly. The constant thickness assumption that is commonly used [11, 16, 29] for wrinkling analysis, is believed to be acceptable in this study based on two reasons, firstly, the strain rate variations due to the change in thickness has limited effects on the material stress-strain behaviours. Secondly, flange wrinkling normally initiates at the early stages of deep drawing, where severe thinning and deformation have not occur. In practical experimentations, for a fully deep drawn part with a draw ratio 1.8 using a flat blankholder ($\alpha = 0$), the minimal and maximum thickness were 1.38 and 1.88 mm respectively, for a temperature of 350 °C, speed of 300 mm/s and blank holding force 10 kN. Hence, the effect of thickness variation when wrinkling occurs can be neglected and the constant thickness assumption is reasonable to be used to simplify the calculation.

$$V_I = \pi H \left(r^{i^2} - (r_P + R_D)^2 \right) \quad (20)$$

$$V_{II} = H\left((\pi^2 - 2\pi)R_D^2 + \pi^2 R_D(r_P + R_D)\right) \quad (21)$$

$$V_{III} = 2\pi r_P H(s - R_D - R_P) \quad (22)$$

$$V_{IV} = H(2\pi R_P^2 + \pi^2 R_P r_b) \quad (23)$$

$$V_V = \pi H r_b^2 \quad (24)$$

where r_p , R_D , r_b, and R_P are radii defined in Fig. 6(b) consistent with the experimental tool dimensions as shown in Fig. 1(b).

Upon inspection, the only volume terms that depend on time are V_I and V_{III}, while others are constant. Then, combining Eqs. (18), (20) and (22), the relationship between the instantaneous radius and forming speed can be obtained by combining Eqs. (18), (20), and (22) to form the following expression.

$$r(t) = \sqrt{\left(r_p + R_D\right)^2 + \frac{1}{\pi H}\left[C - 2\pi r_p H(vt)\right]} \tag{25}$$

where C is defined as follows,

$$C = V_0 - [V_{II} + V_{IV} + V_V + 2\pi r_P H(s_0 - R_D - R_P)] \tag{26}$$

Differentiating Eq. (25) with respect to t gives the following equation.

$$\frac{\partial r(t)}{\partial t} = -\frac{r_P v}{\sqrt{\left(r_p+R_D\right)^2+\frac{1}{\pi H}[C-2\pi r_p H(vt)]}} \tag{27}$$

The strain rate of the fibre at the outer layer, $\dot{\varepsilon}$, in terms of time can be obtained using Eqs (17) and (27).

$$\dot{\varepsilon} = \frac{1}{r}\frac{\partial r(t)}{\partial t} = -\frac{r_p v}{\left(r_p+R_D\right)^2+\frac{1}{\pi H}[C-2\pi r_p H(vt)]} \tag{28}$$

The rate of change of the radius, $\partial r(t)/\partial t$, is negative as the material is undergoing compression. This leads to the strain rate in Eq. (28) being negative to signify compressive strains, however we presented the magnitudes of these variables in our results.

Integrating Eq. (28) with respect to time gives the strain of outer layer of Zone G.

$$\varepsilon = \varepsilon_0 + \frac{1}{2}\ln\left(\frac{C}{\pi H} + \left(r_p + R_D\right)^2 - 2r_P vt\right) \tag{29}$$

where ε_0 is the initial strain which is set to 0 in this study.

The magnitudes of strain rates and strains from Eqs. (28) and (29) are input in the material model and the buckling analysis in the later sections. As seen in Fig. 6(b),

the variables r_p, r_b, R_P, and R_D are dependent on the tool and these are set to be 50 mm, 40 mm, 10 mm, and 10 mm respectively. The value of s_0 was determined from the existing experimental set-up.

3.3.2 Temperature evolution modelling

The hot stamping process is non-isothermal which leads to heat being transferred from the hot work-piece to the cold tools. Additionally, the mechanical properties of aluminium alloys are sensitive to temperature changes. Therefore, the temperature evolution of the material and the temperature effect on the material properties need to be modelled.

The temperature distribution can be described by the energy conservation equation, assuming no mass transfer, radiation, and heat generation, which is given as follows:

$$\frac{\partial T}{\partial t} = \frac{k}{\rho c_p} \nabla^2 T \tag{30}$$

where T is the temperature, k is the thermal conductivity, ρ is the density of the material and c_p is the thermal capacity of the material.

As can be seen in Fig. 7, the part of the work-piece over a groove does not contact the tool and the heat transfer between the blankholder and the work-piece will be most significant at the contact surface. Hence, the heat transfer can be simplified to a one-dimensional system by assuming that the heat is transferred through a single path, firstly in the horizontal direction from the centre of the work-piece to the outer region then vertically from the work-piece to the blankholder. The heat transfer between work-piece and die at Zone G is assumed to be zero compared with that between work-piece and blankholder as the contact pressure is small. Hence, only half of the model is shown in Fig. 7, and the heat transfer paths are illustrated by the red arrows. Due to the axisymmetric geometry feature of tool design and the simultaneous contact between work-piece and tools, the heat transfer in the radial

direction can be neglected for the simplicity of calculation due to the ignorance of air convection and uneven tool surface.

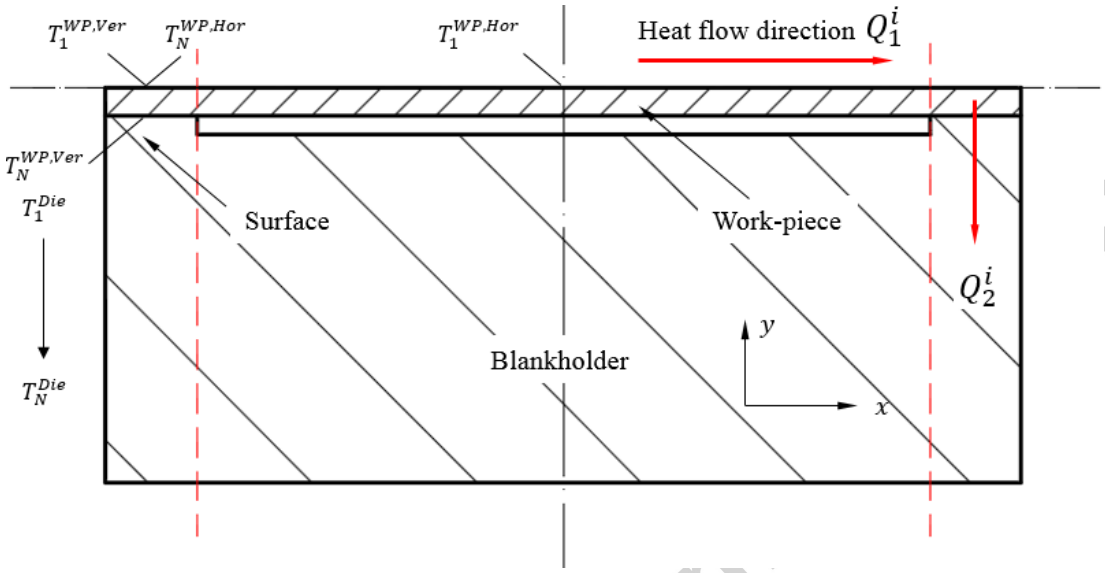

Fig. 7. Schematic diagram of heat transfer between work-piece and tool within one unit (Tool: two surfaces and one groove)

By simplifying the heat transfer into a single path, the differential equation can be simplified as follows.

$$\frac{\partial T}{\partial t} = \beta \frac{\partial^2 T}{\partial s^2} \tag{31}$$

Where s denotes the distance of the heat transfer and

$$\beta = k/\rho c_p \tag{32}$$

The finite difference method was used to solve the partial differential equation, Eq. (31). The difference scheme is shown in Fig. 8.

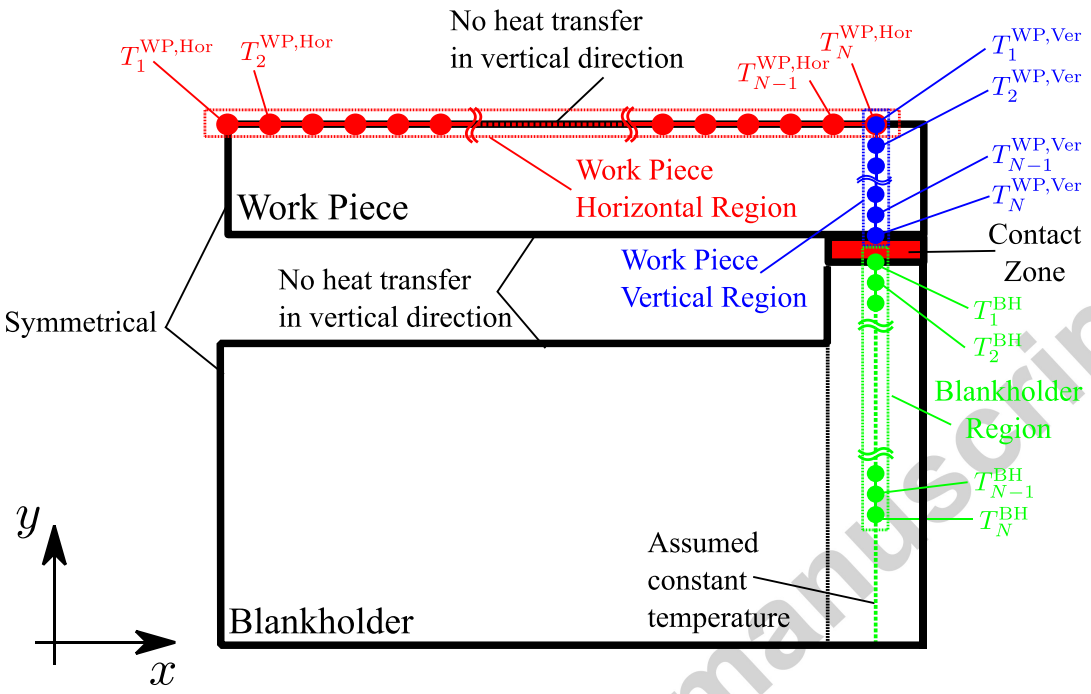

Fig. 8. Definition of regions used for the finite difference calculations

In this study, the backward time-centred space difference scheme, as used in [30], described by Eq. (33) was used.

$$\frac{T_s^t - T_s^{t-\Delta t}}{\Delta t} = \alpha \frac{T_{s-\Delta s}^t - 2T_s^t + T_{s+\Delta s}^t}{\Delta s^2} + O(\Delta t) + O(\Delta t^2) \qquad (33)$$

where O are the truncation error. Neglecting the truncation errors and higher orders, Eq. (33) can be rearranged as:

$$-\frac{\alpha\,\Delta t}{\Delta s^2} T_{s-\Delta s}^t + \left(1 + \frac{2\alpha\,\Delta t}{\Delta s^2}\right) T_S^t - \frac{\alpha\,\Delta t}{\Delta s^2} T_{s+\Delta s}^t = T_s^{t-\Delta t} \qquad (34)$$

From Eq. (34), a matrix for the temperature evolution can be constructed.

$$\boldsymbol{M}\,\boldsymbol{T}^{t} = \begin{bmatrix} * & * & * & * & \cdots & * & * & * & * \\ a_2 & b_2 & c_2 & 0 & \cdots & 0 & 0 & 0 & 0 \\ 0 & a_3 & b_3 & c_3 & \cdots & 0 & 0 & 0 & 0 \\ \vdots & \vdots & \vdots & \vdots & \ddots & \vdots & \vdots & \vdots & \vdots \\ 0 & 0 & 0 & 0 & \cdots & a_{N-2} & b_{N-2} & c_{N-2} & 0 \\ 0 & 0 & 0 & 0 & \cdots & 0 & a_{N-1} & b_{N-1} & c_{N-1} \\ * & * & * & * & \cdots & * & * & * & * \end{bmatrix} \begin{bmatrix} T_1^t \\ T_2^t \\ T_3^t \\ \vdots \\ T_{N-2}^t \\ T_{N-1}^t \\ T_N^t \end{bmatrix} = \begin{bmatrix} T_1^{t-\Delta t} \\ T_2^{t-\Delta t} \\ T_3^{t-\Delta t} \\ \vdots \\ T_{N-2}^{t-\Delta t} \\ T_{N-1}^{t-\Delta t} \\ T_N^{t-\Delta t} \end{bmatrix} \tag{35}$$

where the subscripts denote the node number and the coefficients $a, b,$ and c are given as follows:

$$a = -\frac{\beta\,\Delta t}{\Delta s^2} \tag{36}$$

$$b = 1 + \frac{2\beta\,\Delta t}{\Delta s^2} \tag{37}$$

$$c = -\frac{\beta\,\Delta t}{\Delta s^2} \tag{38}$$

The coefficients in the first and final row of each the matrix in Eq. (35) were set based on the boundary conditions. In this study, the blankholder and work-piece were split into three different regions as illustrated in Fig. 8, which, because of symmetry, illustrates only half the width of the sector between the surfaces. Additionally, the assembly is also symmetrical in the vertical direction, and only half of the blank holder in this direction is illustrated in the Fig. 8. The first region is used to describe the temperature distribution in the horizontal direction of the work-piece and this region is denoted by the superscript, $\mathrm{WP,Hor}$. The second region is used to describe the temperature distribution in the vertical direction of the work-piece, where the work-piece is in contact with the blankholder and this region is denoted by the superscript, $\mathrm{WP,Ver}$. The third region is used to describe the temperature in the vertical direction of the blankholder and is denoted by the superscript BH.

Suitable boundary conditions are needed to determine the temperature distribution of the work-piece and the blankholder. Firstly, the work-piece is assumed to have a uniform temperature initially, which is the forming temperature at $t = 0$. Similarly,

the blankholder is also assumed to have a uniform temperature, which is equal to room temperature at $t = 0$.

For the horizontal trace through the work-piece, due to the symmetry, the temperature gradient, $\partial T/\partial S$, and the heat flux, Q, defined by Fourier's equation. (Eq. (39)) at the right hand end of the work-piece are both zero.

$$Q = -k\frac{\partial T}{\partial S} \tag{39}$$

The temperature at the right-hand end of the horizontal trace is set to be equal to the temperature of the bottom part of the vertical trace in the work-piece.

Similar to the horizontal trace of the work-piece, the heat flux and temperature gradient at the bottom of the vertical trace in the work-piece in Fig. 8, are also equal to zero. The heat flow from the flat die to the work-piece at Zone G in the vertical direction is neglected due to the low interface pressure between the flat die and the work-piece.

The bottom face of the work-piece is in contact with the top part of the blankholder and the heat flux, Q, from the work-piece to the blankholder can be described using the following equation.

$$Q = h\left(T_{Bottom}^{WP,Ver} - T_{Top}^{BH}\right) \tag{40}$$

where h is the heat transfer coefficient.

The heat flux in other regions can also be described by Eq. (40). Lastly, since the blankholder is sufficiently thick, the blankholder is assumed to be of infinite length and this is simulated in the finite difference method by setting the length of the blankholder to be large and setting the bottom node of the blankholder to be constant at room temperature. The discretised expressions of the boundary conditions are as follows.

$$T_2^{WP,Hor} - T_1^{WP,Hor} = 0 \quad (41)$$

$$T_N^{WP,Hor} - T_1^{WP,Ver} = 0 \quad (42)$$

$$T_2^{WP,Ver} - T_1^{WP,Ver} = 0 \quad (43)$$

$$h\left(T_N^{WP,Ver} - T_1^{BH}\right) = -k\frac{\left(T_N^{WP,Ver} - T_{N-1}^{WP,Ver}\right)}{\Delta t} \quad (44)$$

$$h\left(T_N^{WP,Ver} - T_1^{BH}\right) = k\frac{\left(T_2^{BH} - T_1^{BH}\right)}{\Delta t} \quad (45)$$

$$T_N^{BH} = Room\ Temperature \quad (46)$$

The boundary conditions in Eqs. (41) to (46) were substituted into Eq. (35) for each of the individual regions and the equation. is solved for every time step to determine the temperature distribution in the work-piece. The temperatures were then used to calculate the stress-strain values during deformation. Table 4 gives the relevant material and thermal properties used in temperature evolution modelling. The interfacial heat transfer coefficient h is a function of the contact pressure and gap in the hot stamping process, which is obtained using the method developed specifically for the process of hot stamping aluminium alloys [31].

Table 4. Relevant thermal properties

Material	Density ρ g/cm^3	Specific heat c_p $J/(kg \cdot K)$	Thermal conductivity k $kW/(mm \cdot K)$
Work-piece	2.7	890	170
Blankholder	7.8	502	50.2

3.3.3 Modelled Strain Rates and Temperatures

Fig. 9(a) shows the computed results of the relationship between forming speed and strain rate. As can be seen in this figure, the strain rate increases with increasing forming speed, while, the strain rate increases as the flange material is drawn in. Fig. 9 (b) shows the temperature evolution in both work-piece and blankholder. The initial temperature of work-piece is 450 °C and that of blankholder is 20 °C. The X-axis represents the distance between the node and the mid-groove node of hot work-piece, and two intermediate time stages were selected. The temperature of the work-piece decreases rapidly as heat is transferred from the work-piece to the blankholder. This result highlights the importance of accounting for temperature changes in the analysis. Another interesting observation is that the temperature appears to be constant across the thickness of the work-piece, as seen by the horizontal line in Fig. 9(b) at the region that corresponds to the vertical temperature distribution, which suggests that the assumption of treating the work-piece as a one-dimensional system is valid.

Using the model, evolution of strain rate and temperature of work-piece in different regions and at different time stages can be calculated and used as the input parameters for the material model. Hence, the non-isothermal characteristics of the hot stamping process can be captured.

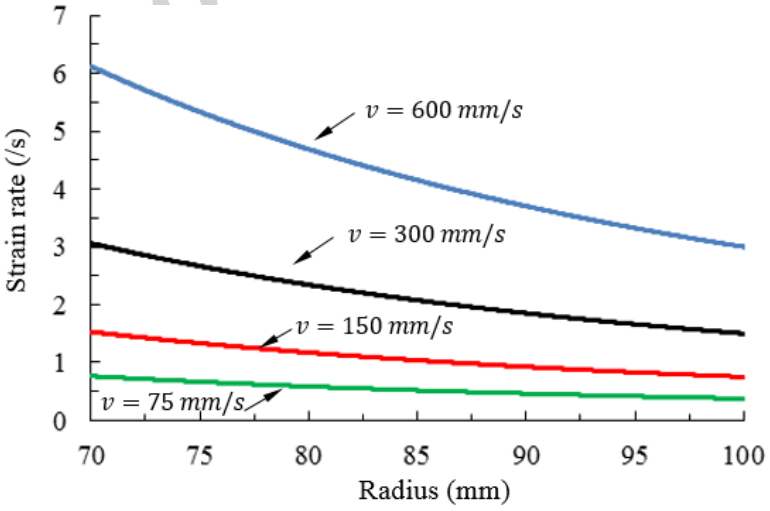

(a) Strain rate evolution during hot stamping

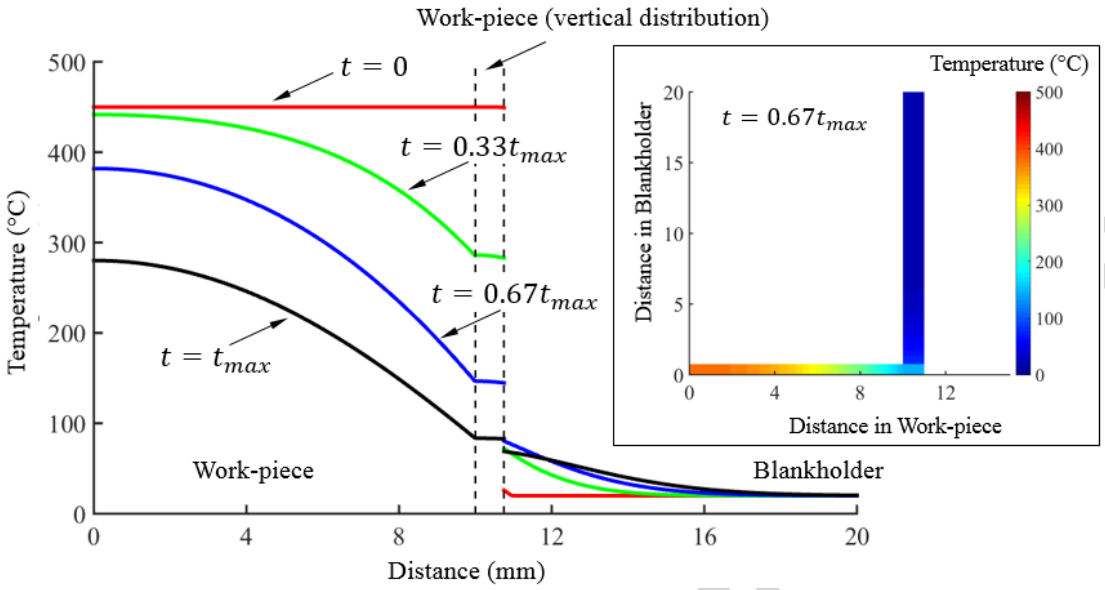

(b) Work-piece temperature evolution during hot stamping

Fig. 9. The evolution of hot stamping process parameters

3.4 Modelling flange wrinkling

The classical energy method was used to establish the buckling model for flange wrinkling of the Zone G material. The Zone G material can be regarded as a one-dimensional beam due to the surface of tool texture constraint. As discussed in Section 3.3.1, the work-piece may buckle at the outer radius of Zone G, which only experiences compressive hoop stress. Therefore, the region where the wrinkling initiates can be assumed to be a uniaxially loaded beam and the one-dimensional (1-D) bucking model using a beam assumption [10] is ideal to determine the onset of wrinkling.

The Zone G material can be regarded as a piece of beam constrained by two surfaces at its ends using the 1-D beam assumption. When the compressive hoop stress $\sigma_{\theta\theta}$

reaches a certain magnitude for a given texture ratio and work-piece draw ratio, the Zone G material experiences buckling according to the classical beam buckling phenomenon as shown in Fig. 10(a). The corresponding beam length is $r_m\theta_G$ in the X-axis, where $r_m = (a + r)/2$, and the Y-axis represents the buckling deflection direction. F^* is the inner force on a particular cross-section when the beam is buckled with a deflection δ. Zheng et al. has found that the hinged boundary condition is more accurate to reflect the tool constraint on the Zone G material [32]. The Senior's energy method [10] is reviewed and applied in this section to analyse the occurrence of Zone G material buckling.

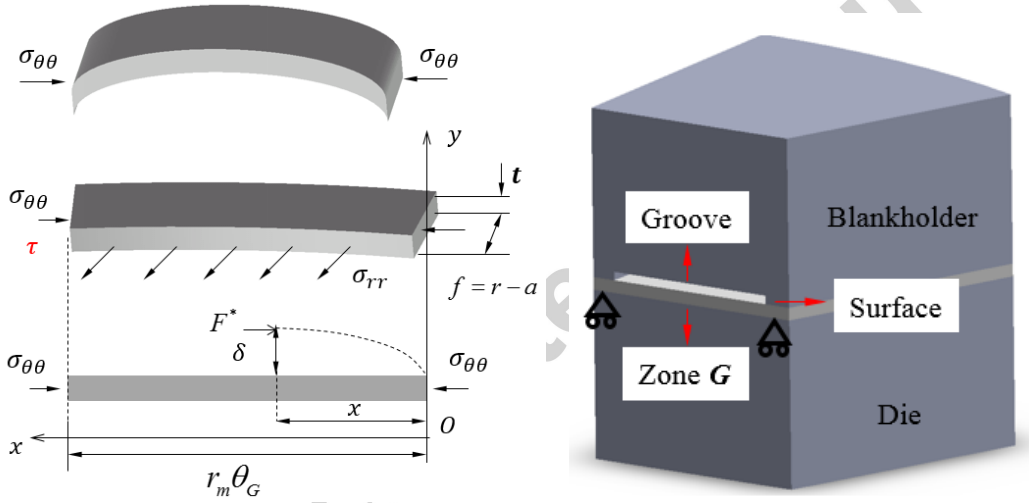

(a) Schematic diagram of beam assumption (b) Hinged boundary condition

Fig. 10. Schematic of assumed beam stresses and the hinged boundary condition [32].

The mathematical expression of the deflection using the hinged boundary condition is given by Eq. (47) satisfying the conditions for the two ends of this assumed beam that: when $x = 0$ and $x = r_m\theta_G$; $y(x) = 0$ and $y''(x) = 0$.

$$y = \delta sin(\pi x/l) \tag{47}$$

where l is the length of a half-wave segment in Eq. (48) with a wrinkling number n, which is assumed as 1 within one unit.

$$l = \theta_G r_m / 2n \tag{48}$$

According to Senior's Euler energy method, the critical condition for buckling is when the energy used to balance the work (ΔT) done by external force is equal to the lateral elastic bending energy, E_B, and the remaining energy, E_P, resulting from tool clamping between punch and die. The limit condition of buckling onset is:

$$\Delta T = E_B + E_P \tag{49}$$

E_B of a half-wave segment of deflection is calculated using Eq. (50):

$$E_B = \frac{1}{2}\int_0^l E_r I \left(\frac{d^2 y^2}{dx^2}\right)^2 \tag{50}$$

where E_r is the reduced modulus proposed by Von Karman to reflect the buckling behaviour in the plastic range given in Eq. (51), I is the second moment inertia $I = ft^3/12$, where $f = r - a$ representing the width of flange material.

$$E_r = \frac{4EE_t}{\left(\sqrt{E}+\sqrt{E_t}\right)^2} \tag{51}$$

where E_t is the material tangent modulus. Substituting Eqs. (47), (48) and (51) into Eq. (50), the expression of E_B can be written as:

$$E_B = \frac{2n^3 E_r I \delta^2 \pi^4}{\theta_G^3 r_m^3} \tag{52}$$

The remaining energy E_P is calculated using Senior's lower limit methods and given in Eq. (53).

$$E_P = \int_0^l \int_0^y f q dy dx \tag{53}$$

where q simulates the tool clamping of inner flange periphery between punch and die.

In Senior's research, the deflection at the mean radius of the flange is proportional to the load as given in Eq. (54) [10]:

$$y = \frac{cqf^5}{8E_r I} \tag{54}$$

where c is a constant.

Substituting Eqs. (47), (48), and (54) into Eq. (53), the expression of E_P is given as:

$$E_P = \frac{fK\delta^2\theta_G r_m}{8n} \tag{55}$$

The work done by the external load, ΔT is calculated as follows:

$$\Delta T = \sigma_{\theta\theta} f t \cdot \lambda \tag{56}$$

where λ represents the moment of load during bending calculated using Eq. (57).

$$\lambda = \frac{1}{2}\int_0^l \left(\frac{dy}{dx}\right)^2 dx \tag{57}$$

Combining Eqs. (47), (48) and Eq. (57), and substituting them into Eq. (56), the detailed expression of the work is given as follows:

$$\Delta T = \sigma_{\theta\theta} f t \frac{n\delta^2\pi^2}{2\theta_G r_m} \tag{58}$$

Then recalling the onset condition of flange wrinkling and substituting Eqs. (52), (55), and (58) into Eq. (49), the detailed expression of the onset condition of plastic buckling in hot stamping condition using hinged boundary condition can be rewritten as:

$$\frac{\sigma_f ln(2r/(r+a))}{E_r} - \left(\frac{t}{f}\right)^2 \cdot \left(\frac{4\pi^2 n^2 (r-a)^2}{3\theta_G^2 (r+a)^2} + \frac{\theta_G^2 (r+a)^2}{24\pi^2 n^2 (r-a)^2}\right) = 0 \tag{59}$$

$$S_{1-D}(\sigma_f, E_r) - G_{1-D}(b, r, t, f, a, n, \theta_G) = 0 \tag{60}$$

where:

$$S_{1-D}(\sigma_f, E_r) = \sigma_f / E_r$$

$$G_{1-D}(r, t, f, a, n, \theta_G) = \left(\frac{t}{f}\right)^2 \cdot \left(\frac{4\pi^2 n^2 (r-a)^2}{3\theta_G^2 (r+a)^2} + \frac{\theta_G^2 (r+a)^2}{24\pi^2 n^2 (r-a)^2}\right) / ln(2\,r/(r+a))$$

3.5 Flange wrinkling determination

According to the onset condition of buckling (Eq. (59)), in addition to the geometry of tool texture and work-piece dimension, the occurrence of flange wrinkling is also related to the material strength, σ_f / E_r, which is dependent on the strain rate and forming temperature. During the hot deep drawing process, strain rate, and temperature vary with time, as modelled in Section 3.3. Therefore, the corresponding parameters, for different stages in the buckling model, need to be obtained to predict flange wrinkling. In this paper, a simple and approximate method [28] is used to establish the relationship between forming and material constitutive equations as shown in Fig. 11. As the flange material experiences the largest compressive stress at the outside edge, wrinkling is assumed to initiate here. A thin slab experiencing uniaxial compression is adopted. In addition, the geometry shape of this piece of material is unchanged and flange material experiences uniform deformation due to the isotropic feature of HFQ® process [8]. Thus, the strain of the material at a given time is determined analytically from Eq. (17) based on the previous analysis.

During a period from t^i to t^{i+1}, the radius of Zone G material varies from r^i to r^{i+1} as shown in Fig. 11(a), the corresponding uniaxial strain can be calculated using Eq. (29), and then the relationships between the work-piece position during drawing and the material strength properties at an instant time can be determined.

To revert a little, Fig. 11(b) shows the fitting of CDM material model developed in Section 3.2 at different temperatures and strain rate 1/s, where the symbols represent

the experimental data obtained from high temperature uniaxial tensile tests [25], and the solid lines represent results from the material model. The tangent modulus E_t^{i+1} for different strain at a given strain rate and temperature can be calculated using Eq. (61).

$$E_t^{i+1} = \frac{\sigma^{i+1} - \sigma^i}{\varepsilon^{i+1} - \varepsilon^i} \tag{61}$$

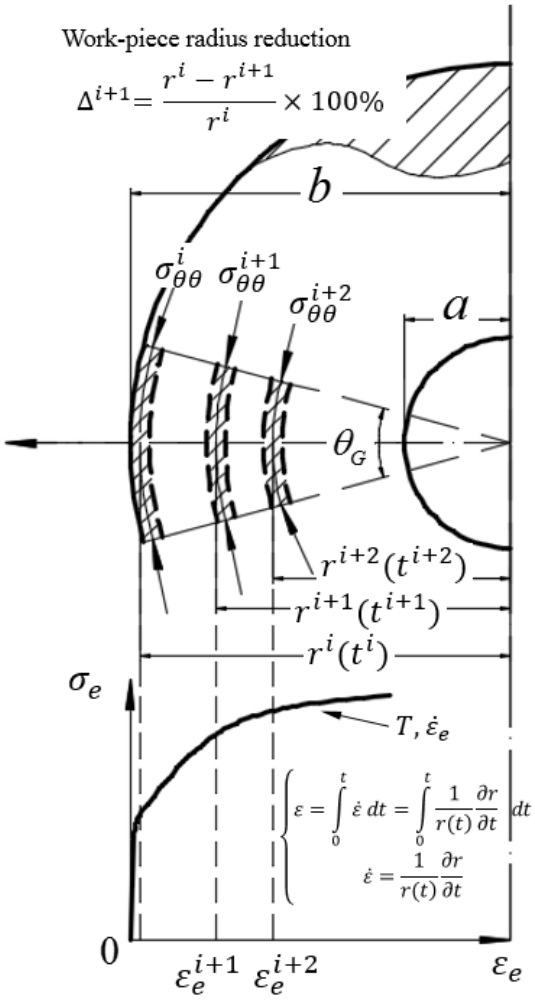

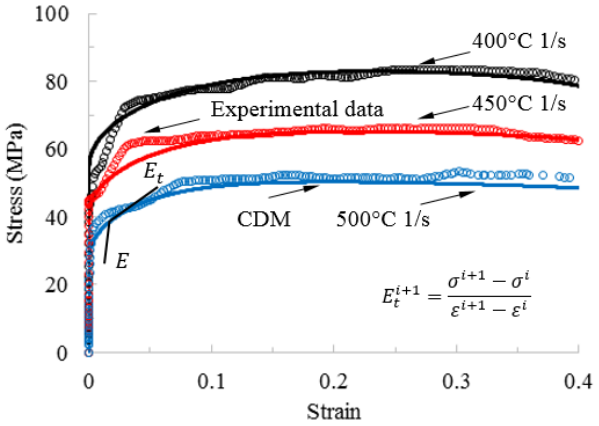

(b) **Fig. 11.** The relationship assumption and material model fitting of the high temperature buckling model (a) The relationship between forming and material stress-strain behaviour (b) CDM material model fitting [25]

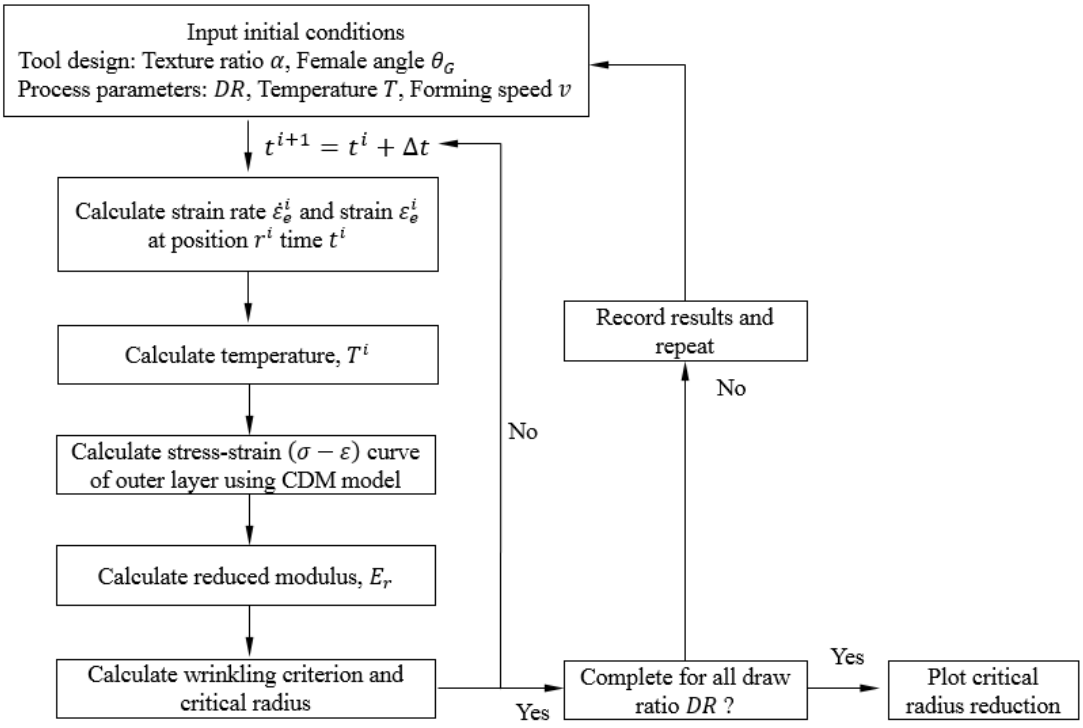

Fig. 12. The flow chart for determining flange wrinkling

Fig. 12 illustrates the complete calculation procedure for determining buckling in the Zone G material. The steps are:

(1) Input all the necessary initial conditions and a time increment ΔT. In this work, Δt is 0.0001.

(2) Calculate the instant radius r^i, strain rate $\dot{\varepsilon}_e^i$ and strain ε_e^i using the modelling in Section 3.3.

(3) Calculate the temperature distribution of Zone G material, in this paper, the temperature of centre node of Zone G was selected to represent temperature input of material model.

(4) Calculate the stress-strain curve of material model using the temperature input and strain rate $\dot{\varepsilon}_e^i$, and calculate the reduced modulus E_r correspondingly.

(5) Determine the wrinkling occurrence using the 1-D buckling model function. If wrinkling occurs, then output critical radius reduction and proceed to the next draw ratio; If not, return to step (1).

4. Results and Discussion

4.1 Experimental validation

In Fig. 13, a comparison of experimental with calculated values of work-piece radius reduction against draw ratio, for different texture ratios, temperatures and forming speeds, are presented. Different tool texture designs are indicated by the shape of the symbols, where the square symbol indicates $\alpha = 3$ and the circle symbol indicates $\alpha = 5$. In addition, solid symbols represent un-wrinkling experimental results that and hollow symbols represent wrinkling experimental results. The solid lines represent calculated critical conditions of wrinkling. The region above the solid line

indicates the wrinkling zone and the region below it indicates no wrinkling. The solid line is referred to as the wrinkling line. As can be seen in Fig. 3(c) and (d), for a wrinkled part, wave wrinkles can be observed on the flange. The wrinkling occurrence was defined when the amplitude of wrinkles reached 1 mm for the experimental results.

As can be seen from Fig. 13(a) to (d), for a given tool texture design, the developed analytical buckling model allows the occurrence of wrinkling to be predicted. Moreover, for different forming temperatures and speeds, the computed critical wrinkling conditions can predict the flange wrinkling with a reasonable error range. Such an error might be caused by the definition of wrinkling occurrence in experimentations and measurement of radius reduction. Experimental wrinkling points are above the wrinkling line, while points for non-wrinkling are below. It should be noted that it is impossible to capture the exact experimental point representing the onset of wrinkling experimentally as this requires precise control of the press stroke that is unachievable with the available equipment. Although the onset of the wrinkling cannot be observed directly from the experiments, some of the results of this study show that the predictions are fairly accurate. The fact that most of the wrinkling points lie above the predicted values, suggests that the model is relatively conservative.

The model developed in this study provides an analytical method for hot stamping aluminium alloys to calculate and determine the flange wrinkling using macro-textured tool designs. Although some simplifications have been made in the modelling process, this work has a huge potential to be further improved to increase its accuracy; this can be done by relaxing several assumptions made in this study or using a more accurate model to determine the buckling criterion. The work can also provide current tool designers with a robust technique to predict wrinkling in hot stamping processes.

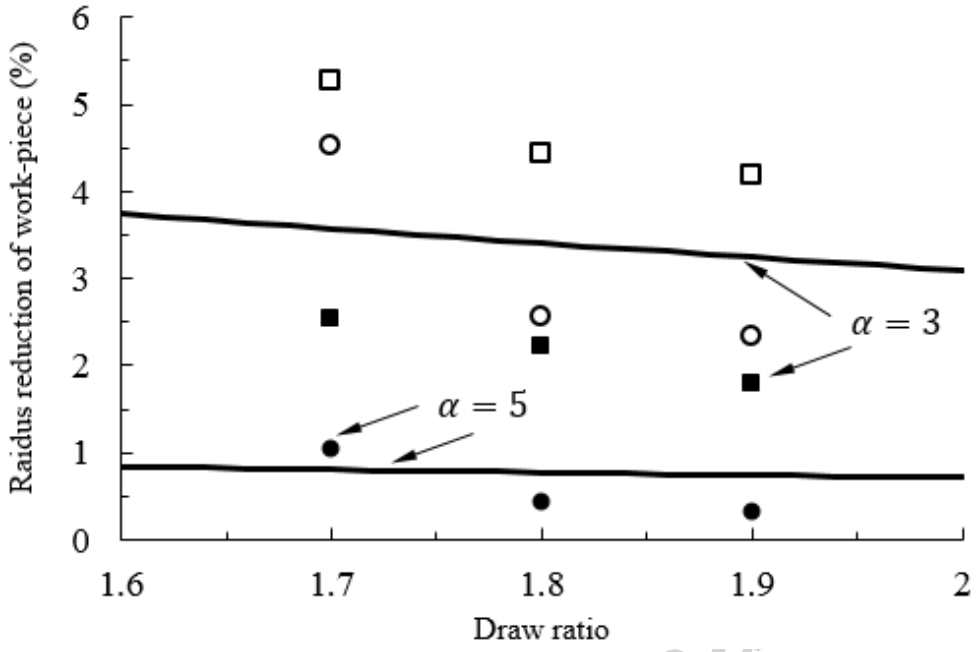

(a) Temperature 350 °C and forming speed 300 mm/s

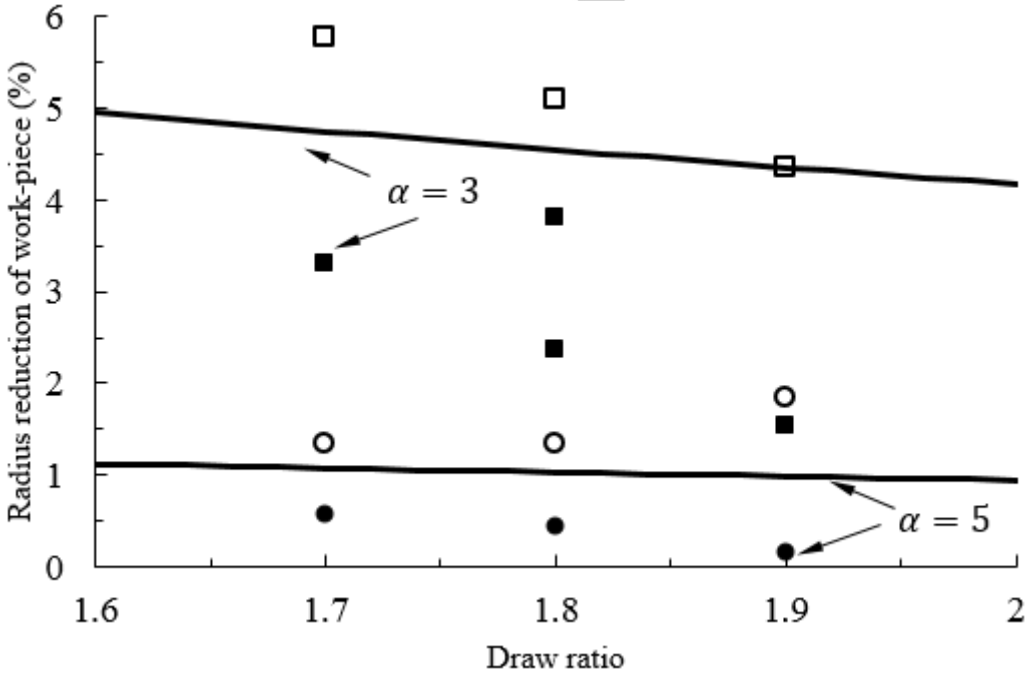

(b) Temperature 450 °C and forming speed 300 mm/s

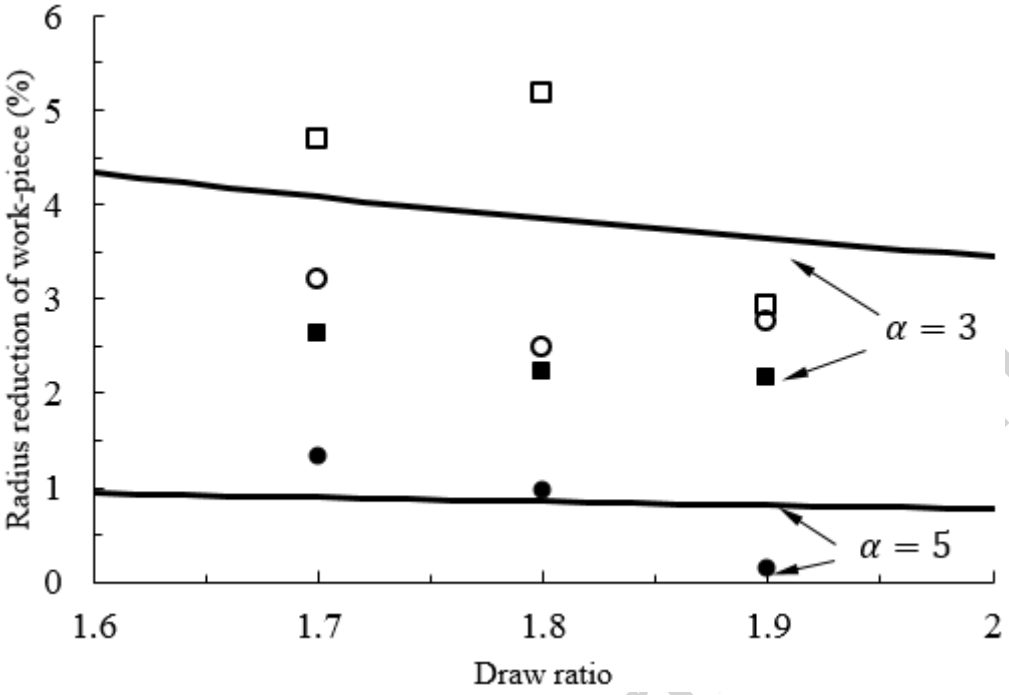

(c) Temperature 350 °C and forming speed 75 mm/s

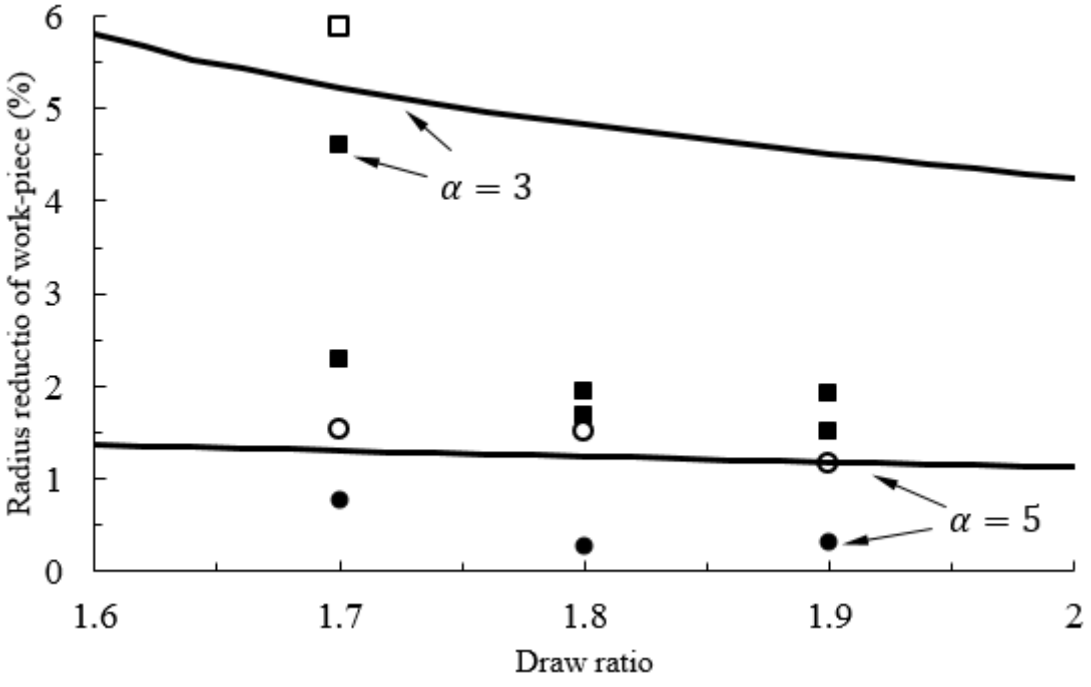

(d) Temperature 450 °C and forming speed 75 mm/s

Fig. 13. Comparison of results from the buckling model (solid lines) and experimentation (symbols). The square symbol indicates $\alpha = 3$ and the circle symbol indicates $\alpha = 5$. Solid symbols represent un-wrinkling experimental results and hollow symbols represent wrinkling experimental results

4.2 Process parameter effects

Unlike the elastic-plastic behaviour of the work-piece material in cold forming processes, the viscoplastic mechanism dominates the work-piece material deformation in hot stamping. This results in forming temperature and speed affecting mechanical properties of the work-piece and resistance to wrinkling, in addition to tool texture geometry and initial work-piece dimension. Fig. 14 shows in detail effects of process parameters on the occurrence of flange wrinkling using the predicted results of the validated buckling model. As the material strength varies with temperature, the forming temperature also affects the resistance of flange wrinkling. Fig. 14(a) shows the effects of forming temperature on the critical condition of wrinkling. For a fixed forming speed of 300 mm/s, resistance to wrinkling increases with increasing initial forming temperature. The reason is that, the magnitude of stress term in the 1-D buckling model, σ_f/E_r , is greater at higher temperatures, as the geometry term G_{1-D} is unchanged, hence, wrinkling phenomenon can be delayed by using higher forming temperatures.

Similarly, resistance to wrinkling can also be increased by increasing forming speed. The reason is believed to be similar to the effects of forming temperature. As the strain rate increases with increasing the forming speed, the work-piece material strength increases with forming speed. Therefore, for the same tool design and initial work-piece dimension, for a particular work-piece material, such as AA6082 used in this study, the magnitude of stress ratio σ_f/E_r term may become greater with increasing forming speed, which causes resistance to wrinkling to be enhanced. It should be noted that, with regard to hot stamping, due to the viscoplastic properties

of the work-piece the stress term σ_f / E_r is determined by the particular grade of alloy as different alloys exhibit different strain hardening and strain rate hardening behaviour at elevated temperatures.

In addition, the effects of initial work-piece draw ratio on the wrinkling occurrence are shown in Fig. 14, the greater the draw ratio, the lower the resistance of wrinkling. This is because the greater draw ratio represents a greater area of the unconstrained Zone G material, hence wrinkling is prone to occur according to Eq. (59). This is similar to what arises in cold stamping processes, as demonstrated by Zheng et al. [32].

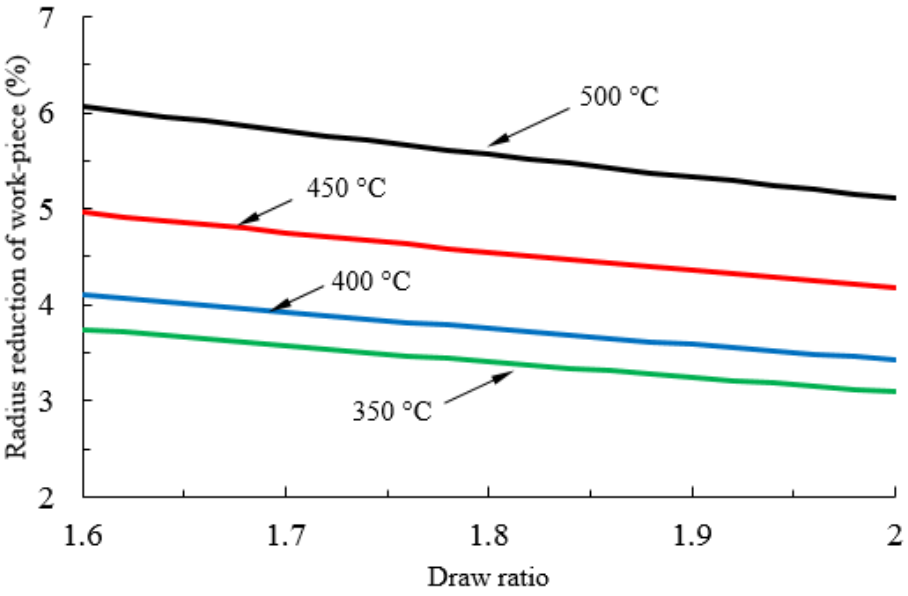

(a) Forming at $v = 300\ mm/s$

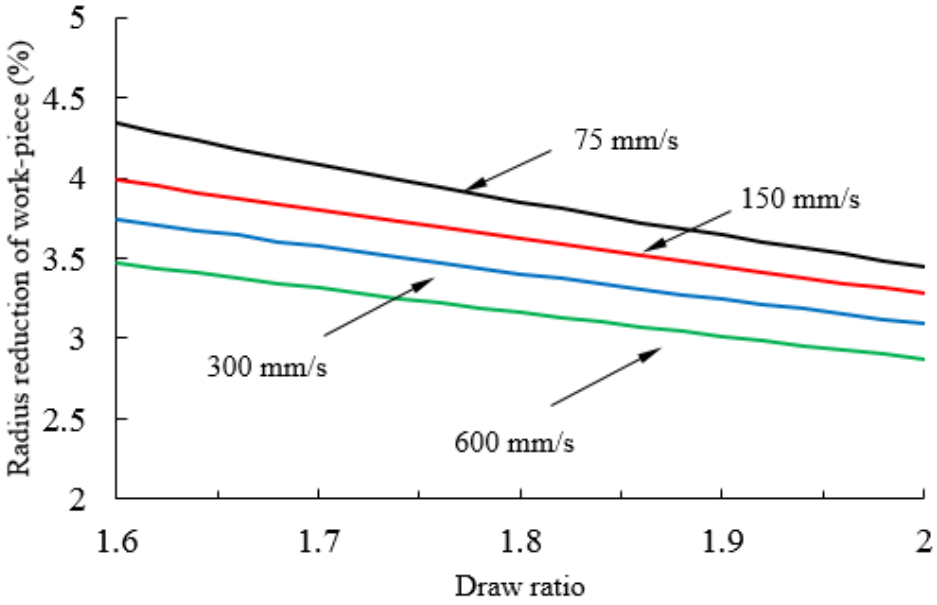

(b) Forming at a temperature of 350 °C

Fig. 14. Effects of process parameters on the wrinkling occurrence for a given tool texture design: $\alpha = 3$

4.3 Texture ratio effects

Both forming temperature and forming speed affect resistance to wrinkling, but the ability to alter wrinkling occurrence using them is limited as the wrinkling process is significantly more sensitive to the texture geometry. Fig. 15 shows the texture ratio effects on the onset of wrinkling at a forming speed 300 mm/s for different work-piece draw ratios at a forming temperature 350 °C. As can be seen in this figure, the resistance of wrinkling increases significantly with decreasing the texture ratio. This observation can be explained as follows. For a smaller texture ratio, the unconstrained Zone G sector becomes much smaller, increasing the magnitude of the geometry term G_{1-D} in the 1-D buckling model to greater than the stress term σ_f/E_r. Hence, wrinkling does not occur easily. The slight flange wrinkling was initiated when the work-piece is drawn at a large radius reduction, which can be eliminated by

the tool ironing and has no effect on the material drawn in as is shown in Fig. 3(a). This slight wrinkling is believed to be caused by the viscoplastic behaviour of material, as can be seen in Fig. 11(b), at elevated temperatures, when the strain reaches a certain magnitude, the softening phenomenon dominates instead of the strain hardening at room temperature, which results in the dramatic decrease of tangent modulus E_t as well as the reduced modulus E_r. Recalling the wrinkling determination equation, Eq. (59), the stress term $S_{1-D}(\sigma_f, E_r)$ becomes smaller and wrinkling is prone to occur. On the contrary, for a larger texture ratio, wrinkling occurs when the work-piece is drawn slightly into the die, and this early occurrence of flange wrinkling can be developed severely with a further work-piece material drawn in.

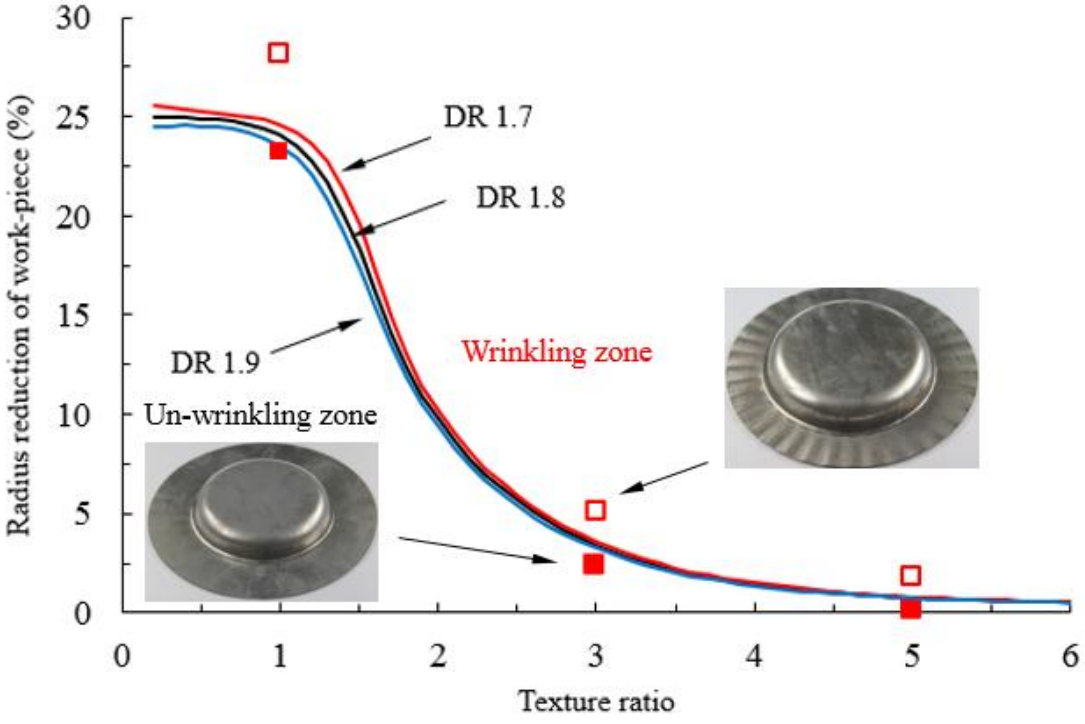

Fig. 15. Effects of texture ratio on the wrinkling occurrence at a forming speed 300 mm/s and temperature of 350 °C

5. Conclusions

The study described in this paper is an investigation of the use of radially grooved, macro-textured tool surfaces in the hot stamping of aluminium alloy. The experimental results show that flange wrinkling occurred in the hollow regions of the texture when the relative groove width reached a certain magnitude for a given process condition. To study this phenomenon, a high-temperature buckling model was constructed, utilising a novel viscoplastic material model for aluminium alloy, which enables the prediction of the onset of wrinkling for different tool texture geometries and different forming conditions. The non-isothermal feature of hot stamping process is captured in this buckling model. The predicted results have shown that, for AA6082, increasing the forming temperature and decreasing the forming speed can enhance the resistance of flange material to buckling but the improvement is relatively modest. Texture ratio and initial work-piece draw ratio are the dominant factors affecting the occurrence of wrinkling. The validated robust buckling model can be a guide for the design of tool features.

6. Acknowledgements

The work described in this paper was supported by the European Commission 7th Framework Programme (Grant agreement no: 604240) as part of the project 'LoCoLite: An industry system enabling the use of a patented materials processing technology for Low Cost forming of Lightweight structures for transportation industries'. Moreover, the contribution of cast and machined tools by Plasmaterm SA are greatly appreciated. The authors would also like to thank the support from Dr. Mohamed S. Mohamed on the material modelling and the China Scholarship Council (CSC) for providing a scholarship to K. Zheng.

References

[1] I.G. Masters, D.K. Williams, R. Roy, Friction behaviour in strip draw test of pre-stretched high strength automotive aluminium alloys, International Journal of Machine Tools and Manufacture, 73 (2013) 17-24.

[2] F. Barlat, Y. Maeda, K. Chung, M. Yanagawa, J.C. Brem, Y. Hayashida, D.J. Lege, K. Matsui, S.J. Murtha, S. Hattori, R.C. Becker, S. Makosey, Yield function development for aluminum alloy sheets, Journal of the Mechanics and Physics of Solids, 45 (1997) 1727-1763.

[3] L. Zhan, J. Lin, T.A. Dean, A review of the development of creep age forming: Experimentation, modelling and applications, International Journal of Machine Tools and Manufacture, 51 (2011) 1-17.

[4] Q.-F. Chang, D.-Y. Li, Y.-H. Peng, X.-Q. Zeng, Experimental and numerical study of warm deep drawing of AZ31 magnesium alloy sheet, International Journal of Machine Tools and Manufacture, 47 (2007) 436-443.

[5] T.A.D. Jianguo Lin, Richard P. Garrett, Alistair D. Foster, Process for forming metal alloy sheet components, in: T.u.o. Birmingham (Ed.), United Kingdom, 2008.

[6] P.F. Bariani, S. Bruschi, A. Ghiotti, F. Michieletto, Hot stamping of AA5083 aluminium alloy sheets, CIRP Annals - Manufacturing Technology, 62 (2013) 251-254.

[7] M.S. Mohamed, A.D. Foster, J. Lin, D.S. Balint, T.A. Dean, Investigation of deformation and failure features in hot stamping of AA6082: Experimentation and modelling, International Journal of Machine Tools and Manufacture, 53 (2012) 27-38.

[8] R.P. Garrett, J. Lin, T.A. Dean, An investigation of the effects of solution heat treatment on mechanical properties for AA 6xxx alloys: experimentation and modelling, International Journal of Plasticity, 21 (2005) 1640-1657.

[9] K. Zheng, D.J. Politis, J. Lin, T.A. Dean, An experimental and numerical investigation of the effect of macro-textured tool surfaces in hot stamping, International Journal of Material Forming, (2015) 1-14.

[10] B.W. Senior, Flange wrinkling in deep-drawing operations, Journal of the Mechanics and Physics of Solids, 4 (1956) 235-246.

[11] T.X. Yu, W. Johnson, The buckling of annular plates in relation to the deep-drawing process, International Journal of Mechanical Sciences, 24 (1982) 175-188.

[12] S.P. Timoshenko, J.M. Gere, Theory of elastic stability, Courier Corporation, 2009.

[13] J. Hutchinson, K. Neale, Wrinkling of curved thin sheet metal, Plastic Instability, (1985) 71-78.

[14] J.W. Hutchinson, Plastic Buckling, in: Y. Chia-Shun (Ed.) Advances in Applied Mechanics, Elsevier, 1974, pp. 67-144.

[15] R. Hill, A general theory of uniqueness and stability in elastic-plastic solids, Journal of the Mechanics and Physics of Solids, 6 (1958) 236-249.

[16] C.-T. Wang, G. Kinzel, T. Altan, Wrinkling criterion for an anisotropic shell with compound curvatures in sheet forming, International Journal of Mechanical Sciences, 36 (1994) 945-960.
[17] F. Barlat, D.J. Lege, J.C. Brem, A six-component yield function for anisotropic materials, International Journal of Plasticity, 7 (1991) 693-712.
[18] E. Chu, Y. Xu, An elastoplastic analysis of flange wrinkling in deep drawing process, International Journal of Mechanical Sciences, 43 (2001) 1421-1440.
[19] J. Cao, A. Karafillis, M. Ostrowski, Prediction of flange wrinkles in deep drawing, Studies in applied mechanics, 45 (1997) 301-310.
[20] J. Cao, Prediction of plastic wrinkling using the energy method, Journal of applied mechanics, 66 (1999) 646-652.
[21] J.L. Chaboche, A review of some plasticity and viscoplasticity constitutive theories, International Journal of Plasticity, 24 (2008) 1642-1693.
[22] O. El Fakir, L. Wang, D. Balint, J.P. Dear, J. Lin, T.A. Dean, Numerical study of the solution heat treatment, forming, and in-die quenching (HFQ) process on AA5754, International Journal of Machine Tools and Manufacture, 87 (2014) 39-48.
[23] V. Franzen, J. Witulski, A. Brosius, M. Trompeter, A.E. Tekkaya, Textured surfaces for deep drawing tools by rolling, International Journal of Machine Tools and Manufacture, 50 (2010) 969-976.
[24] J. Lin, M. Mohamed, D. Balint, T. Dean, The development of continuum damage mechanics-based theories for predicting forming limit diagrams for hot stamping applications, International Journal of Damage Mechanics, 23 (2014) 684-701.
[25] N. Li, Z.T. Shao, J.G. Lin, T.A. Dean, Investigation of Uniaxial Tensile Properties of AA6082 under HFQ® Conditions, in: Key Engineering Materials, Trans Tech Publ, 2016, pp. 337-344.
[26] J. Lin, J. Yang, GA-based multiple objective optimisation for determining viscoplastic constitutive equations for superplastic alloys, International Journal of Plasticity, 15 (1999) 1181-1196.
[27] J. Cao, J. Lin, A study on formulation of objective functions for determining material models, International Journal of Mechanical Sciences, 50 (2008) 193-204.
[28] W. Baldwin, T. Howald, Folding in the cupping operation, ASM TRANS Q, 38 (1947) 757-788.
[29] M. Kadkhodayan, F. Moayyedian, Analytical elastic–plastic study on flange wrinkling in deep drawing process, Scientia Iranica, 18 (2011) 250-260.
[30] Q. Bai, J. Lin, L. Zhan, T.A. Dean, D.S. Balint, Z. Zhang, An efficient closed-form method for determining interfacial heat transfer coefficient in metal forming, International Journal of Machine Tools and Manufacture, 56 (2012) 102-110.
[31] X. Liu, J. Kang, J. Liu, Q. Zhang, L. Wang, Determination of the interfacial heat transfer coefficient in the hot stamping of AA7075, in: MATEC Web of Conferences, EDP Sciences, 2015.

[32] K. Zheng, D.J. Politis, J. Lin, T.A. Dean, A study on the buckling behaviour of aluminium alloy sheet in deep drawing with macro-textured blankholder, International Journal of Mechanical Sciences, 110 (2016) 138-150.

Highlights

- An advanced and analytical buckling model for flange wrinkling in the hot stamping processes of aluminium alloys with macro-textured tools were established the first time.
- The non-isothermal feature of hot stamping process was modelled.
- Hot deep drawing experiments using macro-textured tool surfaces were performed to validate the developed high temperature buckling model.
- The relationships between process parameters and tool textures and flange wrinkling occurrence were analysed.